

Differential Multi-probe Thermal Transport Measurements of Multi-walled Carbon Nanotubes grown by Chemical Vapor Deposition

Qianru Jia, Yuanyuan Zhou, Li Shi

Walker Department of Mechanical Engineering, The University of Texas at Austin, Austin,
Texas 78712, USA

*Email: lishi@mail.utexas.edu

Abstract

Carbon nanotubes (CNTs) are quasi-one dimensional nanostructures that display both high thermal conductivity for potential thermal management applications and intriguing low-dimensional phonon transport phenomena. In comparison to the advances made in the theoretical calculation of the lattice thermal conductivity of CNTs, thermal transport measurements of CNTs have been limited by either the poor temperature sensitivity of Raman thermometry technique or the presence of contact thermal resistance errors in sensitive two-probe resistance thermometry measurements. Here we report advances in a multi-probe measurement of the intrinsic thermal conductivity of individual multi-walled CNT samples that are transferred from the growth substrate onto the measurement device. The sample-thermometer interface thermal interface resistance is directly measured by this multi-probe method and used to model the temperature distribution along the contacted sample segment. The detailed temperature profile helps to eliminate the contact thermal resistance error in the obtained thermal conductivity of the suspended sample segment. A differential electro-thermal bridge measurement method is established to enhance the signal-to-noise ratio and reduce the measurement uncertainty by about 40%. The obtained thermal resistances of multiple suspended segments of the same MWCNT samples increase nearly linearly with increasing length, revealing diffusive phonon transport as a

result of phonon-defect scattering in these MWCNT samples. The measured thermal conductivity increases with temperature and reaches up to $410 \pm 10 \text{ W m}^{-1} \text{ K}^{-1}$ at room temperature for a 7-walled MWCNT and $390 \pm 20 \text{ W m}^{-1} \text{ K}^{-1}$ at room temperature for another 9-walled MWCNT. The obtained thermal conductivity is decreased by a factor of three by organometallic nanoparticles that are deposited on the CNT surface and scatter phonons in the CNT.

Keywords: Carbon Nanotube; Thermal conductivity; Differential thermal transport measurement; Multi-probe device; Chemical Vapor Deposition; Nanomaterials

Nomenclature			
A	Cross-sectional Area (m^2)	Greek	
c	Heat capacity ($\text{J kg}^{-1} \text{ K}^{-1}$)	α	Chiral angle
d	Diameter (nm)	β	Power ratio
G	Thermal conductance (W K^{-1})	\hbar	Reduced plank constant
g	Coupling constant	τ	Relaxation time (s)
h	Distance (nm)	ω	Phonon angular frequency
I	Heating current (A)	θ, ϕ	Temperature (K)
κ	Thermal conductivity ($\text{W m}^{-1} \text{ K}^{-1}$)	Subscript	
L	Length (m)	b	Beam
n_0	Bose-Einstein distribution	c	Contact
Q, q	Heat flux (W)	e	Electrical
R	Thermal resistance ($\text{m}^2 \text{ K W}^{-1}$)	h	High
v	Group velocity (m s^{-1})	i	Inner

w	Width (m)	L	Left
		l	Low
		o	Outer
		R	Right
		s	Surface
		ref	Reference

1. Introduction

As a transport property important for thermal management applications, the solid thermal conductivity of graphitic materials can potentially exhibit peculiar behaviors that deviate from Fourier's law description of diffusive thermal transport. In nonmetallic solids, the thermal conductivity is dominated by the contribution from phonons, the energy quanta of lattice vibration waves. One-dimensional (1D) lattice with simplified interatomic potential can exhibit the Fermi-Pasta-Ulam-Tsingou (FPUT) paradox, for which recurrence of excited phonon modes is accompanied by extremely slow decay of heat flux correlation [1] and a divergence of the effective thermal conductivity (κ) with length (L) according to a power law relationship, $\sim L^\beta$ with $0 < \beta < 1$ [2–4] even at room temperatures. In three-dimensional bulk crystals, in comparison, the divergence is reduced or even removed by elastic anisotropy at low temperatures and by four-phonon scattering at high temperatures[5].

Carbon nanotubes (CNTs) are quasi-one dimensional nanostructures that can behave differently from idealized 1D lattice chains and 3D crystals. A first-principles calculation performed for the defect free single-walled CNT (SWCNT) demonstrates the importance of the

inclusion of both Normal and Umklapp phonon-phonon scattering processes and obtains κ values as high as $6000 \text{ W m}^{-1} \text{ K}^{-1}$ at room temperature[6]. First-order three phonon scattering alone yields a $L^{1/2}$ divergence of the calculated κ of a SWCNT, whereas additional higher-order phonon-phonon scattering results in a saturation of κ when L is over few microns [6–11].

In addition, two recent experiments have reported the observation of second sound, signature of hydrodynamic regime, in graphite at temperatures between about 80 K and 120 K due to strong Normal scattering of flexural phonons in the layered materials[12,13]. Peculiar hydrodynamic phonon transport phenomena can potentially occur in CNTs at an intermediate temperature near 100 K according to a theoretical calculation [14].

These theoretical predictions have attracted interests in fundamental thermal transport investigations and thermal management applications of CNTs. However, current reported experimental thermal conductivity values of individual single-walled (SW) and multi-walled (MW) CNTs vary by one order of magnitude due to the variation of sample quality and limitations and uncertainties in the measurement methods [15–20]. Raman spectroscopy was employed to profile the temperature distribution along the electrically or optically heated suspended CNT samples and extract the contact thermal resistance and resolve the spatial variation of the thermal conductivity[21–24]. Micro-Raman measurements of long suspended CNTs have obtained high thermal conductivity values that saturates to about $2900 \text{ Wm}^{-1} \text{ K}^{-1}$ at room temperature as the length is increased to $10 \text{ }\mu\text{m}$ [20]. Due to the limited temperature sensitivity of the Raman thermometry technique, the sample is often heated by the Raman laser beam by tens of degrees higher than the environment, making it difficult to use this method to measure the thermal conductivity at low temperatures to obtain the temperature-dependent behavior. In comparison, contact thermal resistance errors have been a major issue for past two-probe electro-thermal

microbridge measurement of thermal transport in individual nanotubes. It was previously found that a large contact thermal resistance limited the measured two-probe thermal conductivity of a SWCNT and a double-walled CNT (DWCNT) sample suspended between two microfabricated resistance thermometers to about $600 \text{ W m}^{-1} \text{ K}^{-1}$ at room temperature[25]. Recently, a multi-probe thermal transport measurement has been reported as an effort to measure the contact thermal resistance and the thermal resistance of the suspended segment[26–29]. This method has been used to probe thermal transport of highly defective individual CNTs grown in the nanopores via catalyst-free chemical vapor deposition (CVD) method [30].

Here, we report advancements in multi-probe thermal transport measurements of crystalline multi-walled CNTs grown by high-temperature CVD. The measured interfacial resistance is used in a detailed analytical model of the temperature profile along the contacted sample segment to completely eliminate the contact resistance error and obtain the true thermal conductivity of the suspended segment. A differential electro-thermal bridge measurement method is used to enhance the signal-to-noise ratio and reduce the measurement uncertainty by 40%. The enhanced measurement method reveals effects of surface nanoparticle coating on the thermal conductivity of suspended MWCNTs.

2. Experimental Methods

2.1 Carbon Nanotube Synthesis

Figure 1(a) shows 40- μm -wide trenches that were etched on a Si substrate with the use of Deep Reactive Ion Etching (Deep RIE) [20]. Fe catalyst with about 1 nm thickness was evaporated on one end of the Si substrate. Following a prior report [31], the as-prepared silicon substrate was placed in a 0.3-inch-diameter quartz tube inside the 1-inch-diameter tube furnace to obtain laminar

flow. The stabilized gas flow helps to lift the catalyst nanoparticles at the tip and grow long CNTs via a tip-growth process. After the catalysts were calcinated at 950 °C for 30 min with the H₂ and Ar gas mixture at the flowrates of 10 and 40 sccm, respectively, the CH₄, H₂ and Ar gases were flowed at 950 °C for 3 hrs at the rates of 5, 5, and 40 sccm at atmospheric pressure, respectively. The system was cooled down to the room temperature with the same gas flow. Horizontally aligned ultralong CNTs were grown across the trenches, with the length up to ~100 μm. The diameter of the synthesized CNT is determined by the catalyst nanoparticle size[32].

2.2 Transmission Electron Microscopy (TEM) Measurements

Following the thermal transport measurement, high-resolution transmission electron microscopy (HRTEM) was used to characterize the structure of the suspended MWCNT sample assembled on the multiprobe device (**Figure 1(b)**). According to the TEM measurements (**Figure 1(c)**), the outer diameter of these MWCNTs is in the range of 8.0-13.2 nm and the number of shells varies from 7 to 9, as summarized in **Table 1** for 4 samples. The selected area diffraction pattern (SAED) (**Figure 1(d)**) of sample 1 shows multiple equatorial lines that vary by a few degrees from the average orientation and streaks on spots, indicating the presence of a rotation angel between different layers. A chiral angle α of about 9.2° of one shell of sample 1 can be calculated from the relative distances of the peaks (h_1 - h_3) from the equatorial line in SAED as the following equation [33] and is independent of the scale or a diffraction astigmatism.

$$\alpha = \arctan\left(\frac{1}{\sqrt{3}} \frac{h_2 - h_1}{h_3}\right) = \arctan\left(\frac{1}{\sqrt{3}} \frac{2h_2 - h_3}{h_3}\right) \quad (1)$$

2.3 Non-differential Multi-probe Thermal Transport Measurement

The measurement device in **Figure 1(b)** consists of eight suspended Pd/Cr/SiN_x resistance thermometer (RT) lines. An isolated CNT sample was transferred from the growth substrate with deep trenches onto the microfabricated device with the use of a nanomanipulator. **Figure 1(e)** shows the thermal circuit of the device during the measurement. The measurement is performed with sample in the vacuum space in the cryostat. When a single RT line i is electrically heated at a rate of q_i , the electrical resistances of each RT line j is measured to obtain its temperature rise ($\theta_{j,i}$) based on its temperature coefficient of resistance. A discrete modulated heating and Fourier transform analysis approach is used for sensitive detection of the small temperature rise of a RT line [30]. The measurement is repeated for each RT to be used as the heater line to obtain a set of total $n \times n$ data on $\theta_{j,i}/q_i$, where both i and j run between 1 and $n = 8$ for the eight-probe sample shown in **Figure 1(e)**. This data set can be used to obtain the thermal resistance ($R_{b,j}$) of each RT, the thermal resistance R_j ($j=2$ to 6) and contact thermal resistance $R_{c,j}$ ($j = 2$ to 7) of each inner suspended segment of the nanostructure [30]. Here, the thermal resistance R_j can be separated from the contact thermal resistances because the heat flow across them is different. In comparison, the thermal resistance of the two end segments R_j ($j = 1$ or 8) cannot be identified because the heat flow through the outer segment is the same as that through the corresponding end contact ($R_{c,j}$, $j = 1$ or 8). In addition, the background signal caused by parasitic heat transfer between the heating line and other RTs due to radiation and residual gas molecules inside the evacuated cryostat stage was measured prior to the transfer of the nanotube sample on the multi-probe device. The measured background is then subtracted from the $\theta_{j,i}/q_i$ signal measured on the device with the nanostructure sample to obtain the thermal conductance in the suspended segment of the sample. As in prior works [30], the Joule heating current in the i^{th} line is discretely stepped according to a sinusoidal function. Fast Fourier transform (FFT) data analysis is applied to find the second harmonic

component by analyzing the measured stepped DC heating current and voltage drop in the heating line in addition to the AC voltage drop along other thermometer lines with a small AC sensing current. The FFT results of the sample and background measurement are shown in **Figure 2(a)**.

2.4 Differential Multi-probe Thermal Transport Measurements

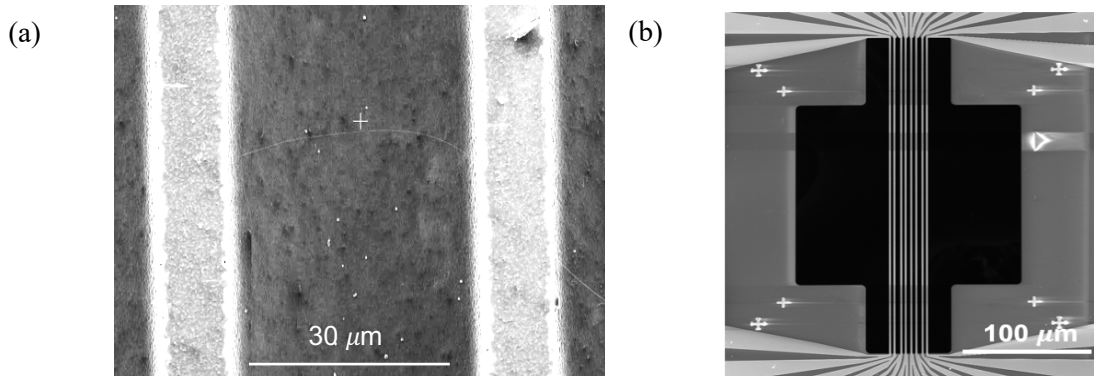
Instead of measuring background signal separately and then subtracting it from the nanotube measurement data to obtain the contribution from the nanotube, in this work we establish a differential multi-probe thermal transport measurement method to eliminate the background thermal conductance during the measurement directly and to enhance the signal to noise ratio. In a prior work [34], a similar differential bridge measurement can achieve a temperature sensitivity of 10^{-4} K by greatly reducing the common-mode noise including substrate temperature fluctuation. The differential measurement obtains the relative increase in the sensing RT temperature for the sample device compared to that for a blank reference device. This increase is caused solely by heat conduction through the nanotube sample. The schematic of the Wheatstone bridge circuit is shown in **Figure 1(f)**. The blank reference device shares the same design as and is adjacent to the sample device on the same chip, except that there is no CNT sample assembled on the reference device. During the differential measurement, the two variable resistors, R_{DC} and $R_{DC,ref}$, are adjusted to achieve the following ratio between the heating currents (I and I_{ref}) in the sample device and the reference device

$$\frac{I}{I_{ref}} = \left[\frac{R_{b,i,ref} R_{b,j,ref}}{R_{b,i} R_{b,j}} \frac{R_{e,i,ref}}{R_{e,i}} \right]^{\frac{1}{2}} \quad (2)$$

where $R_{e,i}$ is the electrical resistance of the i^{th} heater line, the ref subscript is used to differentiate the reference blank device from the sample device, and the beam thermal resistances $R_{b,j}$ is obtained from the non-differential thermal transport measurement for both the sample device and

the reference device. Under this heating condition [34], the same temperature rise ($\theta_{s,j,i}$) would be obtained on the j^{th} RT line of both the sample device and the reference device when the nanotube sample was absent on both devices.

In addition, two lock-in amplifiers are used to measure the difference in the AC voltage drops along the j^{th} sensor lines of the sample and reference devices as $V_s = V_h - V_l$, as shown in **Figure 1(f)**. A variable resistor $R_{AC,ref}$ is used to nullify V_s when there is no DC heating in the two devices. With this balance, the variation of V_s during heating is caused by the different temperature rise on the j^{th} sensing line between the sample and reference devices as a result of heat conduction in the CNT sample. When this differential measurement method is used to test two blank devices without a nanotube sample, the obtained background blank-blank bridge measurement results are compared in **Figure 2(b)** with the sample-blank bridge measurement where the nanotube is assembled on the sample device. The vanishing signal measured on the blank-blank bridge device shows the effectiveness of this method for eliminating the parasitic background and provides an evaluation of the systematic uncertainty of this measurement method, as shown in **Table 2**. Besides being able to correct for the background signal like the nondifferential measurement, the differential bridge measurement improves the signal to noise ratio in the measurement of the small sensor temperature rise caused by heat conduction through the nanotube sample.



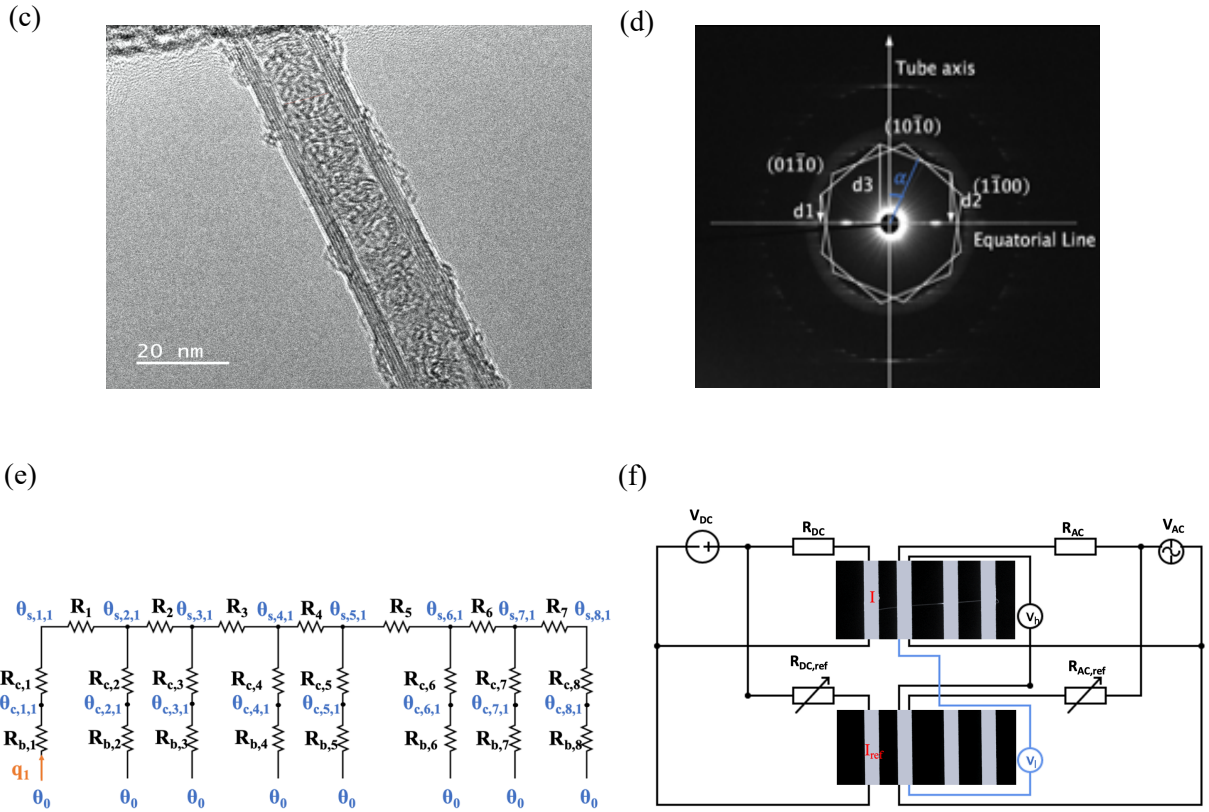


Figure 1. (a) Scanning electron microscopy (SEM) image of an isolated carbon nanotube (CNT) grown across an etched trench in a Si wafer. (b) SEM image of the measurement device that consists of eight 300- μm -long, 2- μm -wide suspended Pd/Cr/SiN_x electrical heaters and resistance thermometers. (c) HRTEM image of MWCNT sample 1 assembled on the multiprobe device. (d) Selected area diffraction pattern for sample 1. The two hexagons represent the first order graphite-like $\{10\bar{1}0\}$ diffraction spots from the top and bottom of the same shell of CNT. Multiple additional spots are visible in the diffraction pattern and indicate that the sample contains multiple shells with different chiral angles. (e) Thermal resistance circuit of the measurement device when the first Pd/Cr/SiN_x line is electrically heated at a Joule heating rate of $(IV)_1$. $R_j, j = 1$ to 7, is the apparent thermal resistances of the j^{th} suspended segments of the suspended sample. $R_{c,j}, j = 1$ to 8 is the contact thermal resistance between the j^{th} Pd/Cr/SiN_x line

and the sample. $R_{b,j}$, $j = 1$ to 8 is the thermal resistance of the j^{th} Pd/Cr/SiN_x resistance thermometer line. $\theta_{c,j,i}$ and $\theta_{s,j,i}$ are respectively the Pd/Cr/SiN_x line temperature rise and average sample temperature rise at the j^{th} contact with the sample when the i^{th} line is electrically heater. The temperature rise θ_0 at the two ends of each of the suspended Pd/Cr/SiN_x lines is assumed to be negligible. (f) Differential bridge measurement setup. A CNT is assembled only on the sample device (top panel) but not on the reference device (bottom panel). The heating to the two devices is adjusted by a variable resistor ($R_{DC,ref}$) so that the sensor temperature rise $\theta_{j,i}$ on the reference device is the same as that of the sample device. Another variable resistor ($R_{AC,ref}$) is adjusted to nullify the AC voltage drop difference across the two sensing lines ($V_s = V_h - V_l$) at zero DC heating voltage ($V_{DC} = 0$).

Table 1 MWCNT sample dimensions measured by TEM . d_i and d_o are the inner and outer CNT diameters, respectively. L_j is the suspended CNT length of j^{th} segment.

Sample	# Shells	d_i/d_o [nm]	L_2 [μm]	L_3 [μm]	L_4 [μm]	L_5 [μm]	L_6 [μm]
1	7	8.5/13.2	8.2	5.0	6.3	2.2	1.0
7	7	8.0/12.2	4.5	2.6	3.3	3.1	7.6
10	9	3.7/9.8	3.0	-	-	-	-
11	9	3.7/9.8	3.0	-	-	-	-

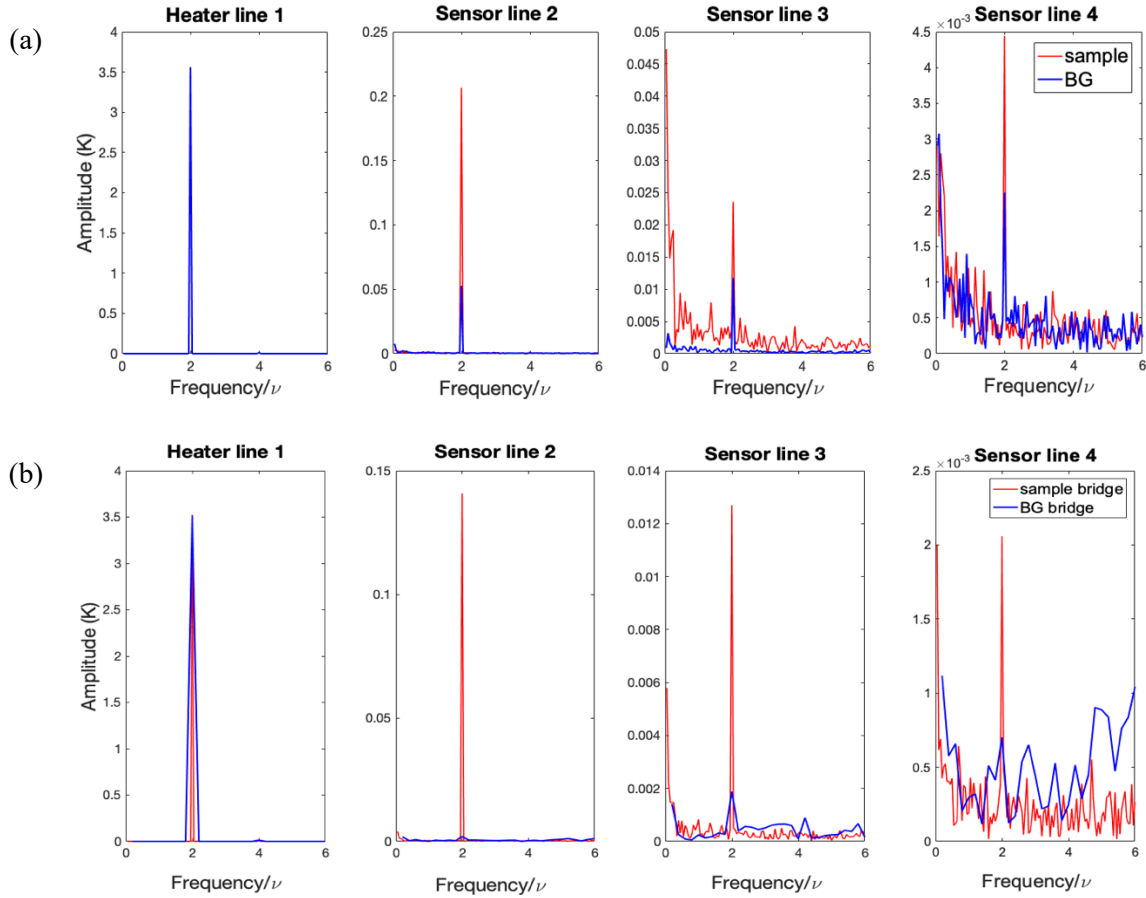


Figure 2. Fast Fourier Transform analysis of measured thermometer temperature modulation from (a) separate non-differential measurements of the sample device (red) and background device (blue), and from (b) differential bridge measurements of a sample-blank bridge (red) and the background blank-blank bridge (blue). Amplitude spectrum of the measured average temperature modulation of each thermometer line is labeled by the thermometer line number in each panel when line 1 is electrically heated at 16 different constant current levels that were cycled to follow a sinusoid at frequency $\nu < 0.025$ Hz for CNT sample 11. The sample stage temperature is 300 K.

Table 2. FFT amplitude of the temperature rises of four-probe measurement devices in both non-differential measurements of a sample and a blank device, differential measurements between

two blank devices, and differential measurements between one sample device and one blank device. The stage temperature is at 300K.

	Heater 1	Sensor 2	Sensor 3	Sensor 4
Sample (K)	3.52	0.207	0.0259	0.00444
Blank (K)		0.0527	0.0117	0.00225
Sample-blank (K)		0.154	0.0142	0.00219
Sample-blank bridge (K)	3.52	0.141	0.0130	0.00206
Blank-blank bridge (K)	3.52	0.000420	0.000694	0.000213
Systematic error		0.298%	8.92%	10.34%

3. Contact Temperature Profile Model

The resistance thermometry measurements obtain the average temperatures rises $\theta_{j,i}$ along each RT line for a given Joule heating rate q_i in the i^{th} heater line. As shown in prior reports [26,30], the measurement data can be used to extract the average contact temperature rises of both the RT line and the nanotube sample, $\theta_{c,j=1 \text{ to } n}$ and $\theta_{s,j=2 \text{ to } n-1}$, where we have eliminated the subscript i used in $\theta_{j,i}$ to represent the heater line. Due to the finite contact length, these average sample temperature rises ($\theta_{s,j}$ and $\theta_{s,j+1}$) at the two adjacent contacts differ from those ($\theta_{L,j}$ and $\theta_{R,j}$) at the left and right ends of the j^{th} supported sample segment. Due to this difference, the measured apparent thermal resistance of an inner suspended sample segment, $R_j = (\theta_{s,j} - \theta_{s,j+1})/Q_j$, still deviates from the actual thermal resistance of the suspended segment, $R'_j \equiv (\theta_{R,j} - \theta_{L,j+1})/Q_j$, where Q_j is the heat flow in the j^{th} suspended sample segment. In addition, due to the different heat current ($Q_{c,j}$) through the contact between j^{th} suspended Pt/SiN beam and the suspended CNT sample compared to Q_j in the adjacent suspended sample segment, $R'_j \neq R_j - R_{c,j} - R_{c,j+1}$.

In this work, we use the measured sample-substrate interface thermal resistance $R_{c,j}$ to model the temperature profile along the supported sample segment and evaluate the R'_j/R_j ratio. The variation of the temperature rise (θ) along the sample segment in contact with the j^{th} thermometer is governed by

$$\kappa_s A \frac{d^2\theta}{dx^2} = g_s A (\theta - \theta_{c,j}) \text{ for } -\frac{w_j}{2} \leq x \leq \frac{w_j}{2} \quad (3)$$

where κ_s is the thermal conductivity of the supported sample segment, w_j is the sample contact length with the j^{th} RT line, A is the sample cross section, and $g_s = (R_{c,j} w_j A)^{-1}$ is the sample-substrate coupling constant. The solution takes the following form

$$\phi = \frac{\phi_{L,j} + \phi_{R,j}}{2 \cosh \frac{w_j}{2L_s}} \cosh \frac{x}{L_s} + \frac{\phi_{R,j} - \phi_{L,j}}{2 \sinh \frac{w_j}{2L_s}} \sinh \frac{x}{L_s} \quad (4)$$

where $\phi \equiv \theta - \theta_{c,j}$, $\phi_{L,j} \equiv \theta_{L,j} - \theta_{c,j}$, $\phi_{R,j} \equiv \theta_{R,j} - \theta_{c,j}$, and $L_s = (\kappa_s/g_s)^{1/2}$ is the sample-substrate thermalization length. The average sample temperature in contact with the j^{th} thermometer line can be obtained from an integration of Equation 4 as

$$\theta_{s,j} = \theta_{c,j} + \frac{L_s}{w_j} (\phi_{L,j} + \phi_{R,j}) \tanh \frac{w_j}{2L_s} \quad (5)$$

We set up the following $2n$ boundary equations to describe continuous heat flow across each junction between the supported sample segment and suspended sample segment

$$-\kappa_s A \frac{d\phi}{dx} = Q_j \quad (6)$$

As the left end and right end of the whole sample are adiabatic,

$$Q_0 = Q_n = 0 \quad (7)$$

At the junction between a supported sample segment and an inner suspended sample segment,

$$Q_j = \frac{\theta_{s,j} - \theta_{s,j+1}}{R_j} \text{ for } j=2 \text{ to } n-2 \quad (8)$$

In comparison, at the junction between the first supported sample segment and the 1st suspended segment,

$$Q_1 = \frac{\theta_{c,1} - \theta_{s,2}}{R_1 + R_{c,1}} \quad (9a)$$

Similarly, at the junction between the n^{th} supported segment and the $(n-1)^{\text{th}}$ suspended segment,

$$Q_{n-1} = \frac{\theta_{s,n-1} - \theta_{c,n}}{R_{n-1} + R_{c,n}} \quad (9b)$$

This set of $2n$ boundary conditions can be arranged into linear equations that can be used to solve for the $2n$ values of $\phi_{L,j}$ and $\phi_{R,j}$. The coefficients in this equation contain the measured values of $(R_1 + R_{c,1})$, $(R_{n-1} + R_{c,n})$, R_j for $j=2$ to $n-2$, and $\theta_{c,j}$ for $j=1$ to n [26,30], as well as the unknown κ_s . Because of the additional substrate-sample phonon scattering that is characterized by a relaxation time (τ_s), κ_s can differ from that (κ) of the suspended sample segment according to

$$\kappa = \sum \tau v^2 \hbar \omega \frac{dn_0}{dT} \quad (10a)$$

and

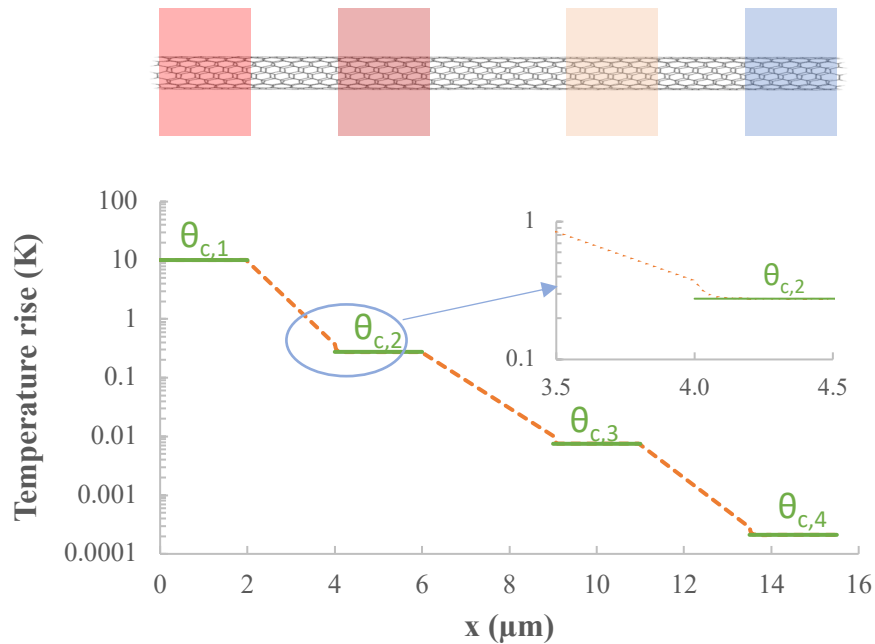
$$\kappa_s = \sum (\tau_s^{-1} + \tau^{-1})^{-1} v^2 \hbar \omega \frac{dn_0}{dT} \quad (10b)$$

Here, the summation is over the wavevector states in the first Brillouin zone, v is the phonon group velocity along the transport direction, \hbar is the reduced Planck's constant, ω is the phonon angular frequency, n_0 is the Bose-Einstein distribution, τ is the phonon relaxation time in the suspended sample segment.

Based on the measured $R_{c,j}$, we obtain $\tau_s = c/g_s$, where the lattice specific heat c is available from lattice dynamical calculation. In the diffusive phonon transport regime, $\kappa = R'_j L_j / A$, with L_j being the length of the suspended sample segment. The temperature-dependent κ can be used to extract the frequency dependent τ , which can then be used together with τ_s to evaluate κ_s . Because the measurement can obtain R_j instead of R'_j directly, an iteration procedure

is used to obtain a new R'_j based on the measured R_j and the R'_j/R_j ratio from the previous iteration step. The new R'_j is then used to evaluate κ , frequency-dependent τ , and κ_s . The obtained κ_s is subsequently used with the other measured values to obtain the values of $\phi_{L,j}$ and $\phi_{R,j}$, which can be used to calculate a new $R'_j/R_j = (\theta_{R,j} - \theta_{L,j+1})/(\theta_{s,j} - \theta_{s,j+1})$. The iteration is completed when the calculated R'_j/R_j converges. **Figure 3(a)** shows the calculated temperature distribution along a multi-walled nanotube sample suspended on four thermometer lines based on this procedure and the measurement results. Due to the large R_j compared to R_b , $\theta_{c,4}/\theta_{c,1}$ is as small as 0.0021% when the 1st RT line is used as the heater line. The inset shows how the nanotube temperature is thermalized toward the contact temperature for the second contact. Accurate measurement of the small temperature signals requires the use of the sensitive differential bridge measurement method.

(a)



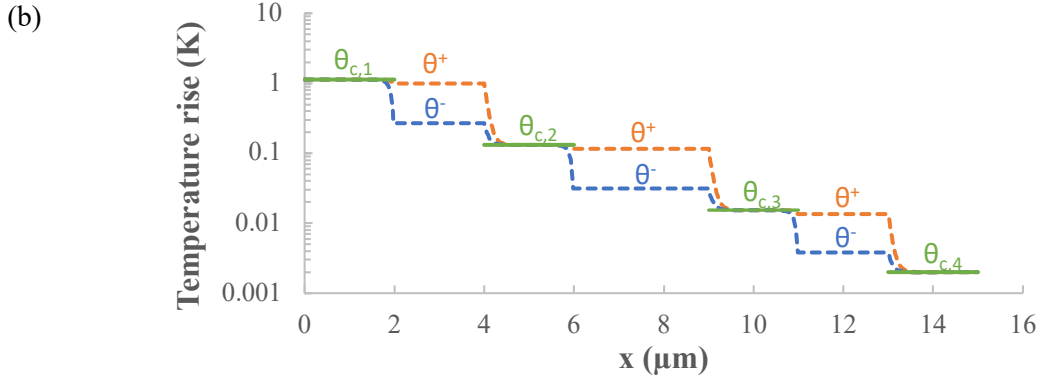


Figure 3. Calculated temperature profiles along (a) a measured diffusive MWCNT sample and a (b) hypothetical ballistic sample suspended on four RT lines.

We note that this model can be further extended to account for ballistic phonon transport in the suspended sample segment, where the right-moving phonons and the left-moving phonons take different temperatures (θ^+ and θ^-) that are spatially invariant along each suspended sample segment. In this case, Equation 4 is expressed separately for θ^+ and θ^- to contain $4n$ values of $\theta_{L,j}^+$, $\theta_{L,j}^-$, $\theta_{R,j}^+$, $\theta_{R,j}^-$. Additional $2n$ boundary equations can be expressed as

$$\theta_{R,j}^+ = \theta_{L,j+1}^+ \text{ and } \theta_{R,j}^- = \theta_{L,j+1}^- \text{ for } j = 1 \text{ to } n-1 \quad (11)$$

The thermal resistance of the suspended ballistic segment is $R_j' = 1/G_b$, where G_b is the ballistic thermal conductance. In addition, $R_j'/R_j = (\theta_{R,j}^+ - \theta_{L,j+1}^-)/(\theta_{s,j} - \theta_{s,j+1})$. **Figure 3(b)** shows the calculated temperature distribution along a hypothetically ballistic nanotube sample suspended over four thermometer lines.

4. Results and Discussion

Several MWCNT samples have been used to establish this measurement method, as listed in **Table 1** For sample 1 that is measured with the use of an 8-probe device and the non-

differential measurement method, the measured R_j increases with the suspended segment length of the MWCNT sample, as shown in **Figure 4**. The deviation of the measurement data from the linear fitting line is generally small and can be attributed to a variation of the crystal quality along different suspended segments. One exception is the data measured at the lowest temperature of 50 K, where the deviation is apparent and the linear fitting extrapolates to a negative number instead of nearly zero for those at higher temperatures. It is possible that quasi-ballistic phonon transport can play a role in the measurement data at 50 K.

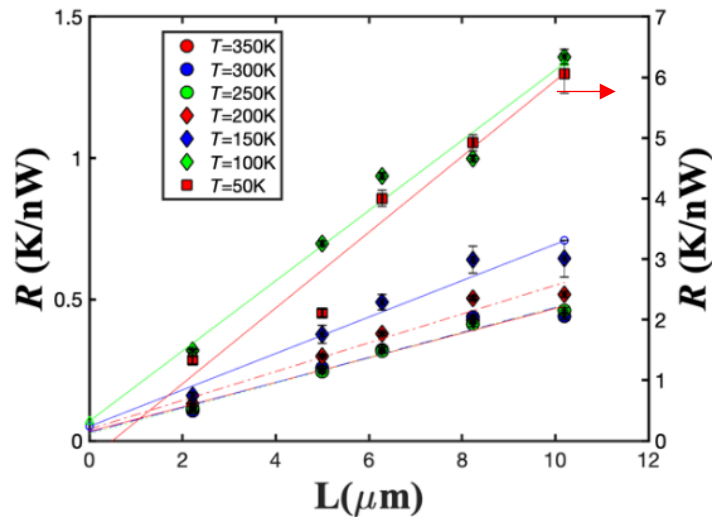


Figure 4. Measured thermal resistances (R_j) of the suspended segments of MWCNT sample 1 as a function of the suspended segment length. The right Y axis is used only for the 50 K data, which shows a larger deviation from the linear fitting line than the high-temperature data.

Among these samples, sample 10 and sample 11 share the same four-probe measurement device design and were both measured via differential and non-differential multi-probe methods. The comparison of the measured thermal resistances of the MWCNT samples as a function of temperature of sample 10 and 11 are shown in **Figure 5 (a, b)**. The results from the differential

and non-differential measurement methods are similar, and show that the contact thermal resistances (R_{c2} and R_{c3}) are more than one-order-of-magnitude smaller than the thermal resistance (R_2) of the middle suspended segment. The differential measurement method obtains an uncertainty that is reduced to $\sim 60\%$ of that obtained from the non-differential measurement for both samples.

Based on these measurement results and the temperature profile model, we obtain that R'_2/R_2 is close to 97.2% and 99.0% for sample 10 and sample 11, respectively. For converting the obtained R'_2 to the thermal conductivity, we calculate the cross section area of the nanotube according to [25]

$$A \equiv \sum_j^m \pi d_j \delta = m\pi\delta[d_1 + (m - 1)\delta] \quad (12)$$

where m is the number of shells of the nanotube, d_j is the diameter of the j^{th} nanotube shell, and $\delta = 3.35\text{\AA}$ is the interplanar spacing of graphite. We note that this interplanar spacing of graphite is very close to the calculated result based on the outer (d_o) and inner (d_i) diameter measurement $(d_o - d_i)/2m$. The difference between this expression from another definition $A = \pi^2(d_o^2 - d_i^2)/4$ is within the reported measurement uncertainty.

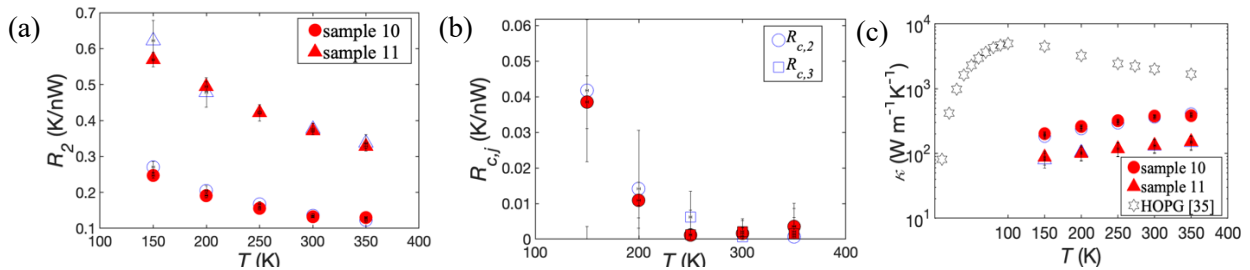


Figure 5. (a) Measured thermal resistances (R_2) of the middle suspended segments as a function of temperature of sample 10 and 11. (b) Measured contact thermal resistances between the middle-suspended CNT segment and thermometer lines of sample 11. (c) Measured thermal

conductivity of the middle suspended CNT segments of sample 10 and 11 as a function of temperature. Also shown for comparison is the highest reported graphite thermal conductivity values (star) included in Touloukian et al. [35]. In all three panels, the data obtained with the differential method and the non-differential method are shown as filled and unfilled markers, respectively.

As shown in **Figure 5(c)**, the obtained thermal conductivity of the suspended middle segment increases with increased temperature and peak at the room temperature. The κ of sample 10 reaches up to $390 \pm 20 \text{ W m}^{-1} \text{ K}^{-1}$ at 300K. Similarly, as shown in **Figure 6(a)**, the κ of sample 7 approaches $410 \pm 10 \text{ W m}^{-1} \text{ K}^{-1}$ at the room temperature. Lower thermal conductivity values are found in the other samples. In comparison, the thermal conductivity of high quality highly oriented pyrolytic graphite (HOPG) samples reach $2000 \text{ W m}^{-1} \text{ K}^{-1}$ at room temperature, and peaks at a temperature near 100 K [35]. The suppressed magnitude and upshift of the peak temperature observed in these MWCNT samples are attributed to extrinsic phonon scattering by defects that dominate intrinsic phonon-phonon scattering in these MWCNT samples.

As shown in a prior work [25], the measured two-probe thermal resistance was decreased by a factor of two after Pt-C was deposited at the contact areas with the use of focused electron beam induced metal deposition. In comparison, the measured intrinsic thermal conductivity of the suspended MWCNT on the multi-probe device is suppressed by nearly a factor of 3 upon similar Pt-C deposition, as shown in **Figure 6(a)**. This opposite result is attributed to the elimination of the contact thermal resistance from the multi-probe measurement in conjunction with the contamination of the nanotube surface by Pt-C particles upon the deposition, as shown in the TEM image of **Figure 6(b)**. The Pt-C particles on the nanotube surface scatter phonons in

the nanotube and reduce its thermal conductivity, similar to scattering of graphene phonons by the substrate in supported graphene[36] and deposited metal coating on suspended graphene [37].

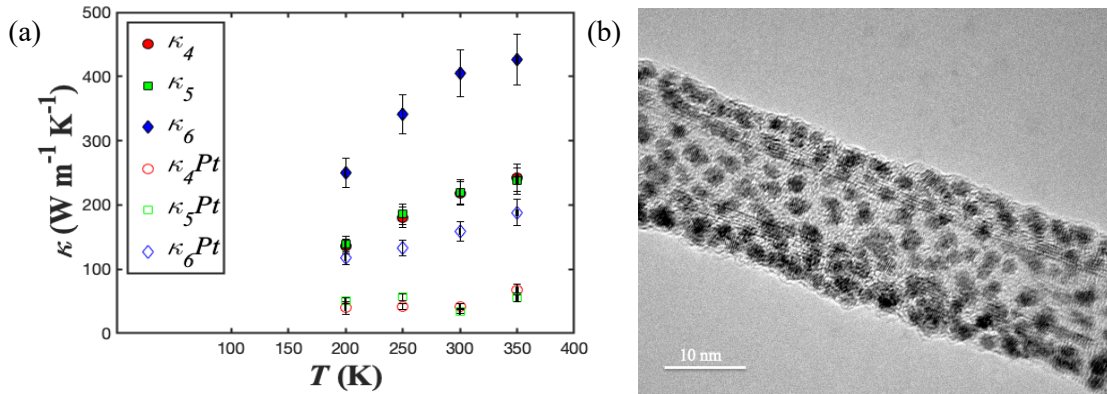


Figure 6. (a) Measured thermal conductivity of the suspended CNT segments as a function of temperature of sample 7 before and after focused electron-beam deposition of Pt-C at the contacts. (b) TEM image of a MWCNT sample 7 coated by Pt-C nanoparticles upon Pt-C deposition.

5. Conclusion

This study makes several advances in multi-probe measurement of thermal transport properties of CNTs. The differential Wheatstone bridge measurement is able to enhance the signal to noise ratio and to reduce the uncertainty to 40% of the non-differential multi-probe measurement. The measured sample-support interfacial resistance is used in an analytical model of the temperature profile along the supported sample segment to fully eliminate the effect of contact temperature drop and obtain the intrinsic thermal conductivity of the suspended segment. As the contact thermal resistance artifact is eliminated, the measured thermal conductivity

reveals a sensitive dependence on the surface coating of nanoparticles. These experimental advances lay the foundation for further experimental probing of the phonon-phonon scattering limited thermal conductivity of high-quality quasi-1D CNTs.

Acknowledgements

The authors thank Karalee Jarvis for helpful TEM discussion. The experiments are supported by National Science Foundation (NSF) award 2015954 from the Thermal Transport Processes Program. QJ was supported by National Science Foundation (NSF) award 1160494 and a University Continuing Graduate Fellowship of the University of Texas at Austin.

Reference:

- [1] E. Fermi, P. Pasta, S. Ulam, M. Tsingou, STUDIES OF THE NONLINEAR PROBLEMS, 1955. <https://doi.org/10.2172/4376203>.
- [2] S. Lepri, R. Livi, A. Politi, On the anomalous thermal conductivity of one-dimensional lattices, *Europhys. Lett.* 43 (1998) 271–276. <https://doi.org/10.1209/epl/i1998-00352-3>.
- [3] O. Narayan, S. Ramaswamy, Anomalous Heat Conduction in One-Dimensional Momentum-Conserving Systems, *Phys. Rev. Lett.* 89 (2002) 200601. <https://doi.org/10.1103/PhysRevLett.89.200601>.
- [4] J.-S. Wang, B. Li, Intriguing Heat Conduction of a Chain with Transverse Motions, *Phys. Rev. Lett.* 92 (2004) 074302. <https://doi.org/10.1103/PhysRevLett.92.074302>.
- [5] I. Pomeranchuk, On the Thermal Conductivity of Dielectrics, *Phys. Rev.* 60 (1941) 820–821. <https://doi.org/10.1103/PhysRev.60.820>.
- [6] L. Lindsay, D.A. Broido, N. Mingo, Lattice thermal conductivity of single-walled carbon nanotubes: Beyond the relaxation time approximation and phonon-phonon scattering selection rules, *Phys. Rev. B.* 80 (2009) 125407. <https://doi.org/10.1103/PhysRevB.80.125407>.
- [7] N. Mingo, D.A. Broido, Length Dependence of Carbon Nanotube Thermal Conductivity and the “Problem of Long Waves,” *Nano Lett.* 5 (2005) 1221–1225. <https://doi.org/10.1021/nl050714d>.
- [8] Z. Wang, D. Tang, X. Zheng, W. Zhang, Y. Zhu, Length-dependent thermal conductivity of single-wall carbon nanotubes: prediction and measurements, *Nanotechnology.* 18 (2007) 475714. <https://doi.org/10.1088/0957-4484/18/47/475714>.
- [9] J.A. Thomas, R.M. Iutzi, A.J.H. McGaughey, Thermal conductivity and phonon transport in empty and water-filled carbon nanotubes, *Phys. Rev. B.* 81 (2010) 045413. <https://doi.org/10.1103/PhysRevB.81.045413>.

- [10] C. Sevik, H. Sevinçli, G. Cuniberti, T. Çağın, Phonon Engineering in Carbon Nanotubes by Controlling Defect Concentration, *Nano Lett.* 11 (2011) 4971–4977. <https://doi.org/10.1021/nl2029333>.
- [11] K. Sääskilähti, J. Oksanen, S. Volz, J. Tulkki, Frequency-dependent phonon mean free path in carbon nanotubes from nonequilibrium molecular dynamics, *Phys. Rev. B.* 91 (2015) 115426. <https://doi.org/10.1103/PhysRevB.91.115426>.
- [12] S. Huberman, R.A. Duncan, K. Chen, B. Song, V. Chiloyan, Z. Ding, A.A. Maznev, G. Chen, K.A. Nelson, Observation of second sound in graphite at temperatures above 100 K, *Science.* 364 (2019) 375–379. <https://doi.org/10.1126/science.aav3548>.
- [13] J. Jeong, X. Li, S. Lee, L. Shi, Y. Wang, Transient Hydrodynamic Lattice Cooling by Picosecond Laser Irradiation of Graphite, *Phys. Rev. Lett.* 127 (2021) 085901. <https://doi.org/10.1103/PhysRevLett.127.085901>.
- [14] S. Lee, L. Lindsay, Hydrodynamic phonon drift and second sound in a (20,20) single-wall carbon nanotube, *Phys. Rev. B.* 95 (2017) 184304. <https://doi.org/10.1103/PhysRevB.95.184304>.
- [15] P. Kim, L. Shi, A. Majumdar, P.L. McEuen, Thermal Transport Measurements of Individual Multiwalled Nanotubes, *Phys. Rev. Lett.* 87 (2001) 215502. <https://doi.org/10.1103/PhysRevLett.87.215502>.
- [16] C. Yu, L. Shi, Z. Yao, D. Li, A. Majumdar, Thermal Conductance and Thermopower of an Individual Single-Wall Carbon Nanotube, *Nano Lett.* 5 (2005) 1842–1846. <https://doi.org/10.1021/nl051044e>.
- [17] E. Pop, D. Mann, Q. Wang, K. Goodson, H. Dai, Thermal Conductance of an Individual Single-Wall Carbon Nanotube above Room Temperature, *Nano Lett.* 6 (2006) 96–100. <https://doi.org/10.1021/nl052145f>.
- [18] C.W. Chang, D. Okawa, H. Garcia, A. Majumdar, A. Zettl, Breakdown of Fourier’s Law in Nanotube Thermal Conductors, *Phys. Rev. Lett.* 101 (2008) 075903. <https://doi.org/10.1103/PhysRevLett.101.075903>.
- [19] H. Hayashi, T. Ikuta, T. Nishiyama, K. Takahashi, Enhanced anisotropic heat conduction in multi-walled carbon nanotubes, *Journal of Applied Physics.* 113 (2013) 014301. <https://doi.org/10.1063/1.4772612>.
- [20] J. Liu, T. Li, Y. Hu, X. Zhang, Benchmark study of the length dependent thermal conductivity of individual suspended, pristine SWCNTs, *Nanoscale.* 9 (2017) 1496–1501. <https://doi.org/10.1039/C6NR06901K>.
- [21] A.W. Bushmaker, V.V. Deshpande, M.W. Bockrath, S.B. Cronin, Direct Observation of Mode Selective Electron–Phonon Coupling in Suspended Carbon Nanotubes, *Nano Lett.* 7 (2007) 3618–3622. <https://doi.org/10.1021/nl071840f>.
- [22] I.-K. Hsu, R. Kumar, A. Bushmaker, S.B. Cronin, M.T. Pettes, L. Shi, T. Brintlinger, M.S. Fuhrer, J. Cumings, Optical measurement of thermal transport in suspended carbon nanotubes, *Appl. Phys. Lett.* 92 (2008) 063119. <https://doi.org/10.1063/1.2829864>.
- [23] I.-K. Hsu, M.T. Pettes, A. Bushmaker, M. Aykol, L. Shi, S.B. Cronin, Optical Absorption and Thermal Transport of Individual Suspended Carbon Nanotube Bundles, *Nano Lett.* 9 (2009) 590–594. <https://doi.org/10.1021/nl802737q>.
- [24] V.V. Deshpande, S. Hsieh, A.W. Bushmaker, M. Bockrath, S.B. Cronin, Spatially Resolved Temperature Measurements of Electrically Heated Carbon Nanotubes, *Phys. Rev. Lett.* 102 (2009) 105501. <https://doi.org/10.1103/PhysRevLett.102.105501>.

- [25] M.T. Pettes, L. Shi, Thermal and Structural Characterizations of Individual Single-, Double-, and Multi-Walled Carbon Nanotubes, *Adv. Funct. Mater.* 19 (2009) 3918–3925. <https://doi.org/10.1002/adfm.200900932>.
- [26] J. Kim, E. Ou, D.P. Sellan, L. Shi, A four-probe thermal transport measurement method for nanostructures, *Review of Scientific Instruments*. 86 (2015) 044901. <https://doi.org/10.1063/1.4916547>.
- [27] J. Kim, E. Fleming, Y. Zhou, L. Shi, Comparison of four-probe thermal and thermoelectric transport measurements of thin films and nanostructures with microfabricated electro-thermal transducers, *J. Phys. D: Appl. Phys.* 51 (2018) 103002. <https://doi.org/10.1088/1361-6463/aaa9d9>.
- [28] E. Ou, X. Li, S. Lee, K. Watanabe, T. Taniguchi, L. Shi, Four-Probe Measurement of Thermal Transport in Suspended Few-Layer Graphene With Polymer Residue, *Journal of Heat Transfer*. 141 (2019) 061601. <https://doi.org/10.1115/1.4043167>.
- [29] B. Smith, G. Fleming, K.D. Parrish, F. Wen, E. Fleming, K. Jarvis, E. Tutuc, A.J.H. McGaughey, L. Shi, Mean Free Path Suppression of Low-Frequency Phonons in SiGe Nanowires, *Nano Lett.* 20 (2020) 8384–8391. <https://doi.org/10.1021/acs.nanolett.0c03590>.
- [30] E. Fleming, F. Du, E. Ou, L. Dai, L. Shi, Thermal conductivity of carbon nanotubes grown by catalyst-free chemical vapor deposition in nanopores, *Carbon*. 145 (2019) 195–200. <https://doi.org/10.1016/j.carbon.2019.01.023>.
- [31] B.H. Hong, J.Y. Lee, T. Beetz, Y. Zhu, P. Kim, K.S. Kim, Quasi-Continuous Growth of Ultralong Carbon Nanotube Arrays, *J. Am. Chem. Soc.* 127 (2005) 15336–15337. <https://doi.org/10.1021/ja054454d>.
- [32] C.L. Cheung, A. Kurtz, H. Park, C.M. Lieber, Diameter-Controlled Synthesis of Carbon Nanotubes, *J. Phys. Chem. B*. 106 (2002) 2429–2433. <https://doi.org/10.1021/jp0142278>.
- [33] M. Gao, J.M. Zuo, R.D. Twisten, I. Petrov, L.A. Nagahara, R. Zhang, Structure determination of individual single-wall carbon nanotubes by nanoarea electron diffraction, *Appl. Phys. Lett.* 82 (2003) 2703–2705. <https://doi.org/10.1063/1.1569418>.
- [34] A. Weathers, K. Bi, M.T. Pettes, L. Shi, Reexamination of thermal transport measurements of a low-thermal conductance nanowire with a suspended micro-device, *Review of Scientific Instruments*. 84 (2013) 084903. <https://doi.org/10.1063/1.4816647>.
- [35] Y. Touloukian, R. Powell, C. Ho, P. eds Klemens, *Thermophysical Properties of Matter, IFI/PLEIMUM • NEW YORK-WASHINGTON*, 1970.
- [36] J.H. Seol, I. Jo, A.L. Moore, L. Lindsay, Z.H. Aitken, M.T. Pettes, X. Li, Z. Yao, R. Huang, D. Broido, N. Mingo, R.S. Ruoff, L. Shi, Two-Dimensional Phonon Transport in Supported Graphene, *Science*. 328 (2010) 213. <https://doi.org/10.1126/science.1184014>.
- [37] J. Wang, L. Zhu, J. Chen, B. Li, J.T.L. Thong, Suppressing Thermal Conductivity of Suspended Tri-layer Graphene by Gold Deposition, *Adv. Mater.* 25 (2013) 6884–6888. <https://doi.org/10.1002/adma.201303362>.